CCFE
CULHAM CENTRE FOR FUSION ENERGY

UK Atomic Energy Authority

UKAEA-CCFE-PR(22)57

S. H. Ward, R. Akers, S. D. Pinches, A. Loarte, R. G. L. Vann, M. A. Van Zeeland, L. Li, Y. Liu, A. Polevoi

# LOCUST-GPU predictions of fast-ion transport and power loads due to ELM-control coils in ITER

# LOCUST-GPU predictions of fast-ion transport and power loads due to ELM-control coils in ITER

S. H. Ward, R. Akers, S. D. Pinches, A. Loarte, R. G. L. Vann, M. A. Van Zeeland, L. Li, Y. Liu, A. Polevoi

This is a preprint of a paper submitted for publication in Nuclear Fusion

# LOCUST-GPU predictions of fast-ion transport and power loads due to ELM-control coils in ITER

**S. H. Ward**

York Plasma Institute, Department of Physics, University of York, York YO10 5DD, UK
Culham Centre For Fusion Energy, Culham Science Centre, Abingdon, OX14 3DB, UK
ITER Organization, Route de Vinon-sur-Verdon, CS 90 046, 13067 St. Paul Lez Durance Cedex, France

**R. Akers**

Culham Centre For Fusion Energy, Culham Science Centre, Abingdon, OX14 3DB, UK

**A. Loarte**

ITER Organization, Route de Vinon-sur-Verdon, CS 90 046, 13067 St. Paul Lez Durance Cedex, France

**L. Li**

College of Science, Donghua University, Shanghai 201620, China

**Y. Q. Liu**

General Atomics, P.O. Box 85608, San Diego, California 92186-5608, USA

**S. D. Pinches**

ITER Organization, Route de Vinon-sur-Verdon, CS 90 046, 13067 St. Paul Lez Durance Cedex, France

**A. R. Polevoi**

ITER Organization, Route de Vinon-sur-Verdon, CS 90 046, 13067 St. Paul Lez Durance Cedex, France

**R. G. L. Vann**

York Plasma Institute, Department of Physics, University of York, York YO10 5DD, UK

**M. A. Van Zeeland**

General Atomics, P.O. Box 85608, San Diego, California 92186-5608, USA

E-mail: samuel.ward@york.ac.uk

**Abstract.**

The LOCUST-GPU code has been applied to study the fast-ion transport and loss caused by resonant magnetic perturbations in the high-performance $Q = 10$ ITER baseline scenario. The unique computational efficiency of the code is exploited to calculate the impact of the ITER ELM-control-coil system on neutral beam heating efficiency, as well as producing detailed predictions of the resulting plasma-facing component power loads, for a variety of operational parameters—the toroidal mode number $n_0$, mode spectrum and absolute toroidal phase of the imposed perturbation. The feasibility of continually rotating the perturbations to reduce the RMS power loads is assessed. In addition, the implementation of 3D magnetic fields in LOCUST is also verified by comparison with the SPIRAL code for a DIII-D discharge with ITER-similar shaping and $n = 3$ perturbation.

Continuous rotation of the perturbation is found to reduce RMS fast-ion power loads. However, careful adjustment of the perturbation phase may make this unnecessary, as peak power loads are found to correlate with reductions in NBI heating efficiency for $n = 3$ fields. Adjusting the phase this way can increase total NBI system efficiency by approximately 2-3% and reduce peak power loads by up to $0.3\,\mathrm{MWm^{-2}}$. Overall, $n = 3$ fields are preferred to $n = 4$ from the point of view of fast-ion confinement.

## 1. Introduction

The ITER tokamak aims to operate in high-confinement mode (H-mode) [1] to achieve high-gain ($Q \sim 10$), long-pulse ($\sim$ 1000s) plasma discharges [2]. However, the additional power expelled during the type-I edge-localised modes (ELM) typically observed in H-mode plasmas poses a risk to both plasma performance and reactor longevity in ITER-scale devices [3]. To mitigate or suppress ELMs, ITER is equipped with a set of ELM-control coils (ECC) that impose resonant magnetic perturbations (RMP) onto the plasma, breaking the underlying equilibrium axisymmetry.

Experimental and computational studies have suggested that RMPs lead to the transport of fast ions [4]. Particles are predicted to be mostly affected where the RMP amplitude is greatest, often at the edge of the plasma, where the neutral beam injection (NBI) coincidentally deposits an intense, anisotropic source of fast ions. Hence many studies corroborate the risks that ECCs pose to NBI ions in particular—specifically, the resulting reduction in beam ion confinement, NBI heating efficiency and associated increase in power flux to plasma-facing components (PFC). All of these risks must be managed if ITER is to achieve its aims.

The distribution of the PFC power flux is thought to be dictated by the influence on fast-ion orbits by the various magnetic structures that exist within the RMP field [5][6][7][8][9]. These structures are influenced in turn by the design and operation of the ECCs [10]—that is, the geometry of each coil and current it passes—in combination with the plasma's response to the produced RMP [11][12], which may screen [13] or even amplify the RMP field [4] and resulting transport [12]. Therefore, the potential risk that ITER's high-power NBI system (up to 33 MW initially [14]) poses to the PFCs [15] (designed to tolerate up to 10 $\mathrm{MWm^{-2}}$ maximum at the divertor, less elsewhere [16]) could be aggravated or mitigated depending on how the ECC system is operated. This potential optimisation is why the ongoing study of ECC operation, plasma response models, and their combined influence on the PFC power flux is advocated in support of the ITER research plan.

Despite the importance of this topic, it remains challenging to study computationally due to the extreme scale of the ITER device. Kinetic fast-ion codes which hope to accurately resolve PFC heatloads must cope with a huge spatiotemporal domain (one second slowing down time, $\sim$ $800\mathrm{m}^3$ plasma volume), model expansive yet intricate wall geometries, and resolve fine structures in RMP fields. This bottlenecks attempts to systematically simulate the ITER system without significant computational resources, making the optimisation problem difficult. However, the LOCUST code [17] is a novel kinetic fast-ion algorithm that is designed to make reactor-scale systems tractable on desktop hardware. Whilst this could potentially provide a way of discovering new physics, in this context LOCUST also enables the routine study of ITER at high fidelity, allowing for precise optimisation—for example through the minimisation of localised, component-specific heatloads.

This paper aims to evaluate methods of mitigating reductions in NBI heating efficiency and localised PFC power loads due to ECCs by predicting the related fast-ion transport in ITER. The distribution of lost NBI power is calculated for $n_0 = 3$ and $n_0 = 4$ ECC waveforms, which oscillate to rotate the RMP toroidally whilst maintaining ELM suppression. To resolve the PFC power at the component level, we use the LOCUST code to model fast-ion dynamics in the presence of detailed and realistic models of the first-wall and RMP field. Because of this, we also verify the implementation and convergence of the 3D magnetic field model in LOCUST.

After describing and testing the 3D magnetic field model in section 2, the ITER ECC system, and the physical model used to represent it, is described in section 3. Section 4 then presents the results of studying this model with LOCUST, including the measured fast-ion transport and PFC power loads at different RMP phases. Finally, section 5 presents a summary and outlook of the work.

## 2. 3D magnetic fields in LOCUST

LOCUST is a high-performance kinetic fast-ion code. It utilises hardware acceleration via programmable graphics processing units (GPU) and tuned software algorithms to massively parallelise the calculation of fast-ion slowing-down trajectories at speeds unachievable with traditional central processing unit (CPU) codes. This allows for the efficient, full-orbit tracking of large populations (millions) of markers over long periods of time (seconds). For this reason, the code is uniquely suited for calculating fast-ion transport and detailed PFC power loads in ITER.

To ensure accuracy when extrapolating to ITER, a device not yet studied experimentally, we tested the implementation of 3D magnetic fields in LOCUST. The code has previously been shown [17] to compare well with other fast-ion codes and experiment in a variety of scenarios with axisymmetric plasmas, including those with ITER-similar shapes such as DIII-D shot #157418 [7]. Here we study #157418 again, including the $n_0 = 3$ RMP applied during the discharge.

Using the same plasma input data from [7], the corresponding results from LOCUST were compared to the simulations presented in [7] by SPIRAL [18]. SPIRAL

is a widely accepted code that is regularly used in comparisons with experiment. Though SPIRAL's speed and reliance on conventional CPU hardware makes it unable to study ITER at high fidelity without significant computational resources, its wide use makes the code very well-suited for verification exercises. LOCUST used a higher precision version of the perturbed field and plasma response calculated by M3D-C1 [19], generated on a grid with 3.7 mm spacing to ensure convergence. LOCUST used the same neutral beam deposition as SPIRAL, which was generated by beams injected both co and counter to the plasma current, including all three energy components as well as the effects of the plasma displacement on the temperature and density profiles due to the applied RMP.

Figures 1 and 2 show the changes in the steady-state fast-ion distribution function, $f$, caused by the RMP. The distribution function is cropped to include only the plasma edge, in regions satisfying $\rho > 0.77$, where $\rho$ represents the square root of the normalised toroidal flux. Though this cut-off is different in [7], where $\rho > 0.7$, the small volume within $0.7 < \rho < 0.77$, and the resulting influence of finite bin-widths, means manual tuning was required to capture this sensitive region. Figure 1 shows the difference between $f$ calculated with and without the 3D magnetic field, $f_{3D}(\epsilon, \lambda) - f_{2D}(\epsilon, \lambda)$, as a function of energy $\epsilon$ and particle pitch angle $\lambda = v_{\parallel}/v$ measured against the plasma current. There is good qualitative agreement between the codes; both show transport in the same region of phase space, corresponding to edge-localised, co-passing particles. Of these particles, those with energies above 40keV—half injection energy—are affected somewhat differently between the simulations. Figure 2 illustrates this more clearly, showing the RMP-induced transport as a fraction of the axisymmetric distribution function, $[f_{3D}(\lambda) - f_{2D}(\lambda)]/f_{2D}(\lambda)$. The effect of these high-energy markers is a 10% point difference in the transport within $0.8 < \lambda < 1.0$, $\epsilon > 40$keV. This could be because SPIRAL, unlike LOCUST, extends the electron density profile past the last-closed flux surface, generating increased drag at higher energies for edge-localised markers. Likewise, LOCUST did not include plasma rotation, impurities or electric fields. Both 2D and 3D representations of the first-wall were used in LOCUST to gauge the effects of wall model variations. Compared with SPIRAL, which uses a 3D representation, the variations are small.

Nevertheless, these results show that there are no detectable errors in LOCUST's implementation of 3D magnetic fields.

## 3. ITER ELM-control coil fields

### *3.1. The ITER ECC system*

The ITER ECC system is illustrated in Figure 3. It will consist of three rows of nine, regularly spaced window frame coils, with centres starting at $\phi = 30°, 26.7°$ and $30°$ for the upper, middle and lower rows respectively. Each coil is independently powered and consists of six windings passing a maximum of 15 kA each (90 kAt total magnetomotive force) [20]. To impose RMPs of a given fundamental toroidal mode number, $n_0$, each ECC will operate with a current defined by

$$I(\phi_{\text{coil}}) = I_0 \cos(n_0[\phi_{\text{coil}} - \Phi] - \omega t), \quad (1)$$

where $\phi_{\text{coil}}$ is the toroidal location of the coil centre, $\omega$ ($\approx 5$ Hz [3]) is a rotational frequency and $\Phi$ defines a toroidal phase shift—typically applied to each coil row independently to alter the poloidal spectrum of the 3D magnetic field. From an operational point of view, $I_0$, $n_0$, $\Phi_{\text{u,m,l}}$, $\omega$ are the controllable degrees of freedom, subject to the operational limitations and a desired level of ELM suppression. It is worth noting that the toroidal spectrum of an RMP imposed by coils of finite width and number is often largely composed of harmonics higher than the fundamental toroidal mode number, $n_0$, where the spectrum $n$ is made up of $n_0, n_1$ etc. For example, the ratio of amplitudes of the first and second harmonics are approximately 70-85% for $n = 3, 6$ and 88-95% for $n = 4, 5$ in ITER, depending on the coil geometry (which differs between rows). Importantly, these additional harmonics, which sometimes rotate counter to the coil current profile and fundamental harmonic, lead to variations in the poloidal spectrum throughout rotation—potentially altering the fast-ion dynamics and resulting PFC footprint. Typical spectra for ITER are illustrated in Figure 4.

### *3.2. RMP and plasma model*

The 3D magnetic fields created by the ITER ECC system used herein have been calculated previously [21][22]. The plasma response was calculated by MARS-F [23][24] using plasma parameters determined by ASTRA [25] under various assumptions of plasma Prandtl number (ratio of toroidal momentum to thermal diffusivity in the core) and ratio of toroidal momentum to thermal confinement times—$(\tau_\phi/\tau_E)$. Together, these affect the plasma rotation at the core and edge respectively, in turn influencing the plasma's ability to screen the external perturbation. For the fields used in this study, the differences in rotation act only to scale the overall response amplitude without affecting the perturbation structure—though the increase in amplitude is small. If anything, this amounts to linearly scaling the total fast-ion losses [26].

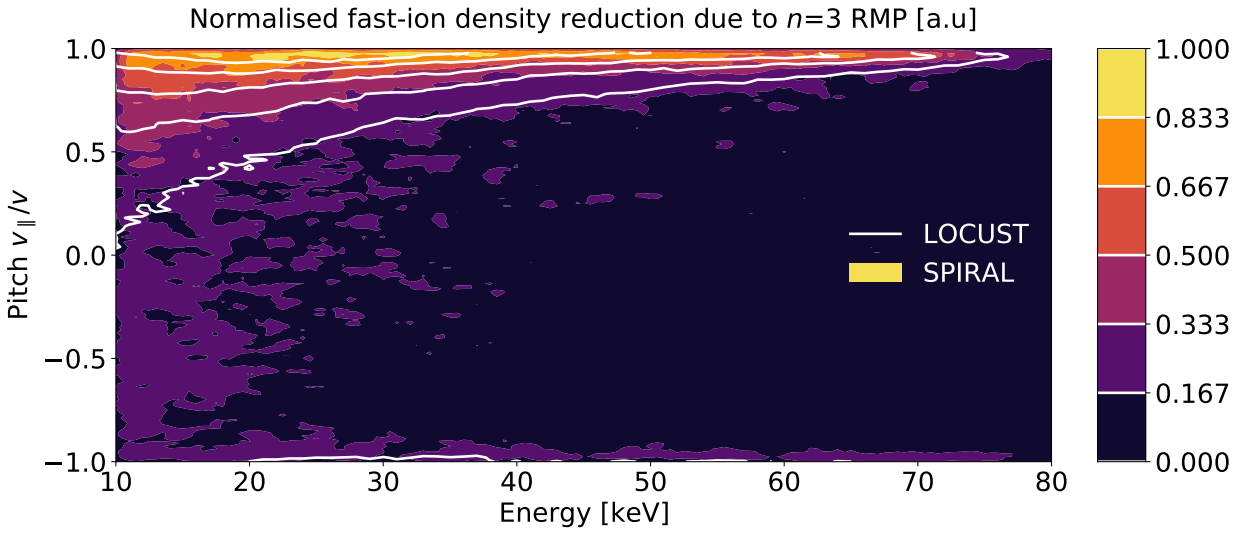


**Figure 1.** The normalised, element-wise difference—$\delta f(\epsilon, \lambda)$—between $f(\epsilon, \lambda)$ calculated with and without a pure $n = 3$ RMP field, where $f(\epsilon, \lambda)$ is the distribution function integrated over all dimensions except energy and pitch. Filled contours are calculated by `SPIRAL` whilst the white intermediate contours by `LOCUST`. A perfect match corresponds to white contours perfectly defining the boundaries between the filled contours. In both simulations the RMP leads to transport in the same region of phase space, whilst quantitative discrepencies are limited to high energies and are caused by physics unlreated to the 3D magnetic field model.

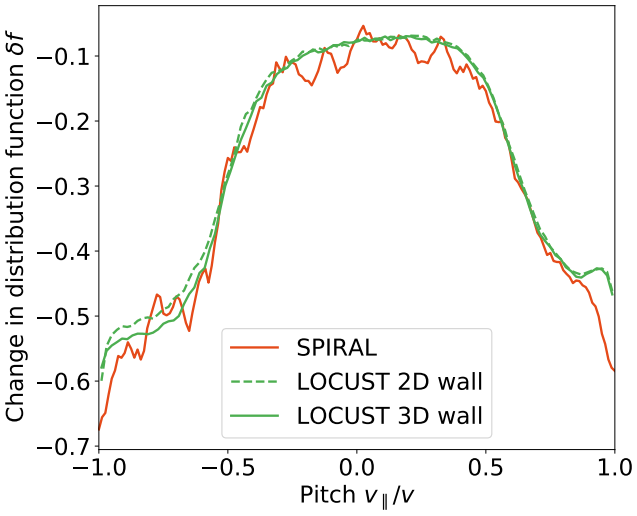


**Figure 2.** The element-wise difference, $\delta f(\lambda)$, expressed as a fraction of $f_{2D}(\lambda)$ calculated without the RMP field. Included are results from `LOCUST` simulations using a simple 2D outline for the axisymmetric wall and a defeatured CAD model for the 3D wall. The small difference at high pitch can be explained by differences in the electron drag—not differences in the 3D magnetic fields.

The fields used here are based on equilibria calculated assuming $\tau_\phi/\tau_E = 2$ and a Prandtl number of 0.3 [27], which correspond to a smaller X-point displacement amplitude (XPD), due to the relatively high toroidal rotation [28]—which is still predicted to be small in ITER (10-30 kRad/s).

The fields calculated by `MARS-F` are decomposed into toroidal harmonics for each coil row and are accessible via `mhd_linear` interface data structures (IDS) in the ITER integrated modelling and analysis suite (`IMAS`). `mhd_linear` IDSs are storage containers native to ITER's IMAS software ecosystem that enforce a data schema, allowing for the storage and exchange of simulation data between physics codes. This allows for simulating an arbitrary level of ELM suppression by linearly rescaling, combining and phase-shifting the fields from individual coil rows prior to reading by `LOCUST`. The total field is then generated by interpolating to a Cartesian $R - Z$ grid, where high-order splines are used near the separatrix region to resolve the fine structures created by thin current sheets. As this may be different to methods used in other fast-ion codes, Figure 5 shows a simple convergence test to gauge the required grid precision. The NBI power loss was calculated over multiple simulations in which only the perturbation grid spacing changed. $\nabla \cdot \mathbf{B}$ was evaluated and averaged over all points within the plasma, before being scaled by one of two lengths: $B$ on-axis and either the Boris step length at the injection energy or the perturbation grid spacing, the latter of which should give an estimate of the global truncation error. As the grid size is reduced, the global error decreases like $\mathcal{O}(\Delta x_{\widetilde{\mathbf{B}}})$. Convergence of fast-ion losses begins below 10 cm, however it takes until $\approx 3$ cm for fast-ion losses to stabilise. Therefore, a grid size of 1 cm was chosen.

A similar convergence test was also performed for particle time step, with the time distribution of losses converging for a Boris step of $\approx 1$ ns. Finally, losses were found to near saturation after $\approx 30$ ms, which

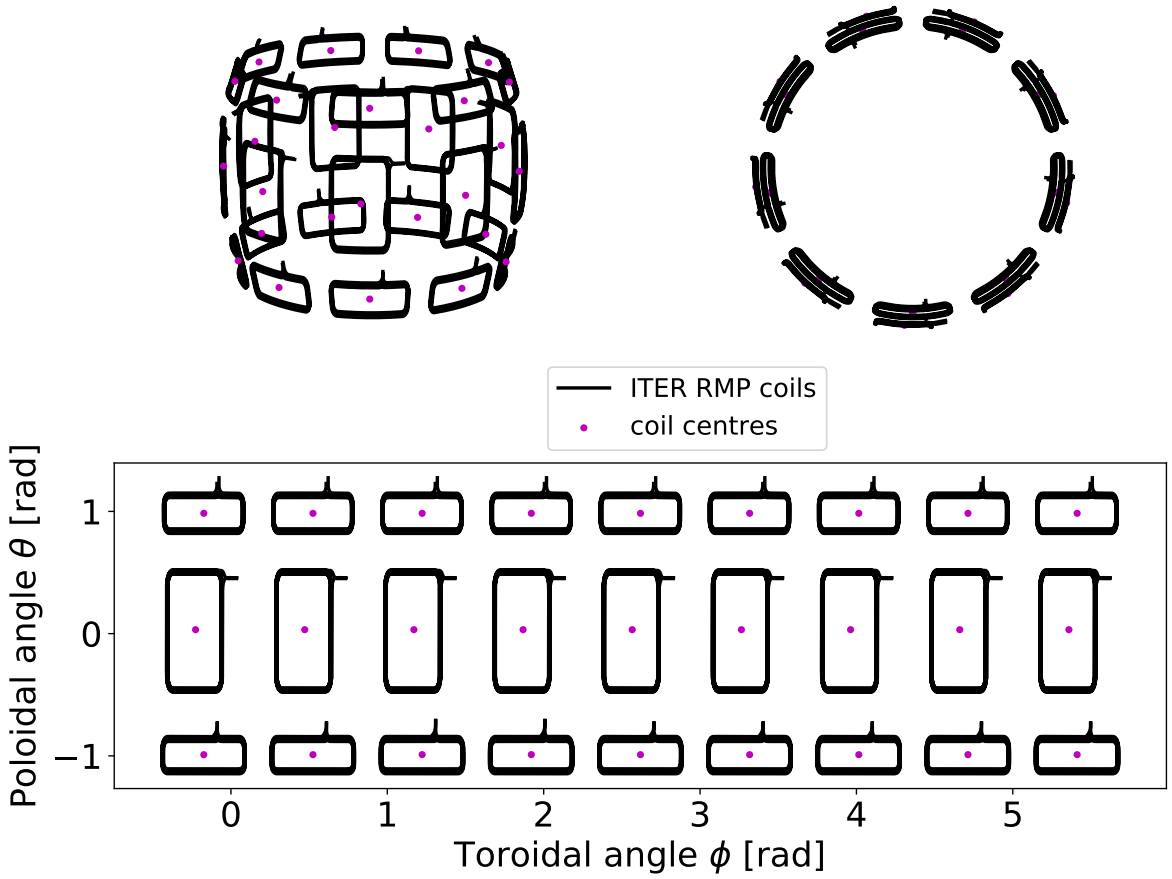


**Figure 3.** Top left: View of the the ITER ECC system (not to scale). The three rows of rectangular coils are responsible for imposing 3D perturbations onto the plasma by each passing a current defined by equation 1. Top right: View looking on the ECC system from above. Coil spacing is toroidally symmetric within a given rown, but offsets exist between rows. Importantly, all coils are positioned on the outboard side of the plasma, meaning that the power deposited by heating systems must be transmitted through the RMP field. Bottom: Distribution of ECC coils in poloidal ($\theta$) and toroidal ($\phi$) angle. Coil centres are marked in magenta in all subplots. The finite poloidal and toroidal width of each coil is responsible for the presence of significant higher harmonics in the RMP spectrum.

was then used as a time cut-off in all simulations. It was therefore assumed that the time-dependent fast-ion losses due to an ECC system oscillating at 1-10 Hz could be well-approximated by separate simulations using static RMP fields at discrete phase intervals; i.e. we approximate $\omega = 0$.

For consistency, the same axisymmetric equilibrium and plasma parameters, such as temperature and density profiles, used in `MARS-F` from `ASTRA`, were also used here by the collision operator in `LOCUST`. No specific model was used to extend the plasma into the scrape-off layer (SOL). For simplicity, and due to observing a negligible effect on high-energy fast-ion losses, impurities were ignored. The `BBNBI` [29] `IMAS` actor was used to calculate a realistic fast-ion deposition from the heating neutral beam system into the axisymmetric equilibrium plasma. Finally, a volumetric mesh (57.6M tetrahedra) derived from a defeatured computer-aided design (CAD) model of ITER was used to represent the first-wall geometry. This mesh is detailed enough to resolve the under-dome cooling pipes, as well as the subtler geometrical features of larger components, such as the the gaps between divertor cassettes and the shaped surfaces of the first-wall tiles. Gaps exist for heating and diagnostic ports. This is illustrated in Figure 6, which shows the PFC geometry and its individual components highlighted.

## 4. Fast-ion power loads in FPO discharges

The simplest method of optimising fast-ion transport in ITER is to adjust the absolute phase of the applied RMP. Experiments suggests that rotation of RMP fields modulates the intensity of fast-ion power flux on a given PFC—for instance, a fast-ion loss detector (FILD) [7][30]. Whilst this suggests RMP phase may

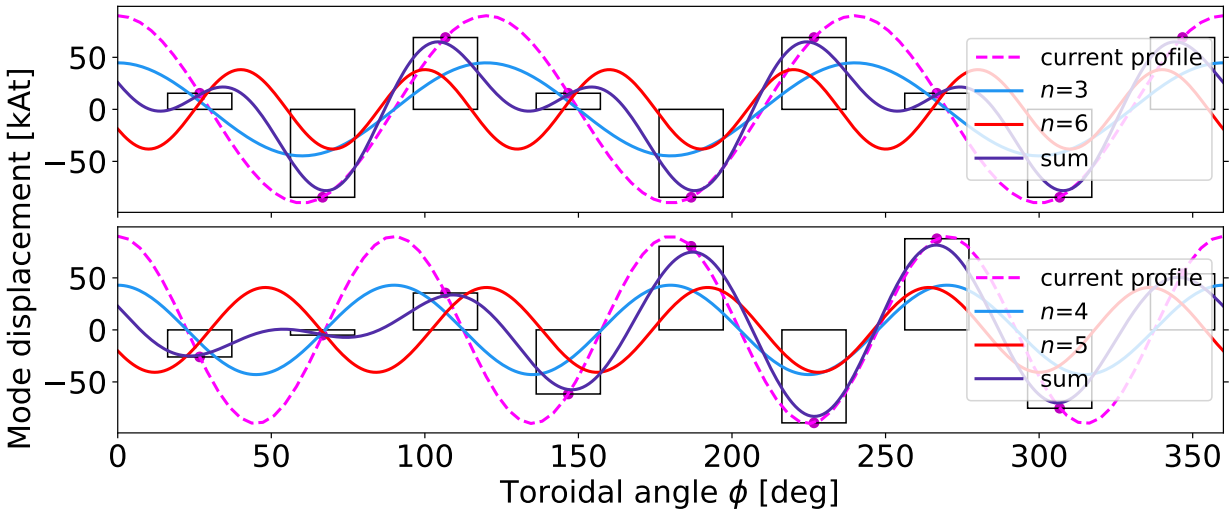


**Figure 4.** Current distribution (magenta) defined by equation 1 for $n_0 = 3$ and $n_0 = 4$ RMPs in ITER ECCs (black quadrangles where height represents current passed), as well as the first two corresponding harmonics (blue, red) and their sum (purple), for $\Phi = 0$. The pink scatter points serve as visual guide to confirm that the ECC centres adhere to the magneta current profile. In both cases, the finite number of coils means the higher harmonic significantly contributes to the total waveform.

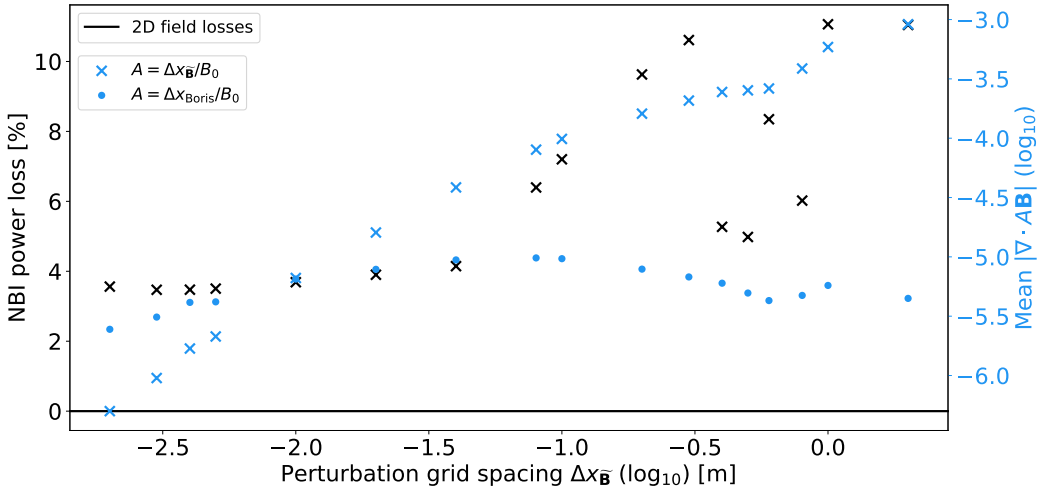


**Figure 5.** Perturbation grid spacing convergence test measuring global fast-ion losses, as a percentage of deposited beam power, along with the average magnetic divergence, $\nabla \cdot \mathbf{B}$, scaled according to two length scales: the perturbation grid spacing and a typical marker step length. To show the underlying 2D equilibrium is sufficiently resolved, the global losses in the axisymmetric field, which are expected to be negligible, are also shown. The beginnings of convergence in global truncation error and particle losses co-incide at approximately 10 cm, with both decreasing approximately linearly. Losses saturate at roughly 3 cm; to give some margin for error, a grid spacing of 1 cm subsequently then chosen for all simulations.

be used to control where the power flux lands, it may also modulate the global loss rate. Therefore, one may choose to optimise the RMP phase according to some combination of maximising total NBI heating efficiency and minimising peak PFC power fluxes to avoid localised melting. In both cases, an optimal RMP phase could be determined and fixed. However, if large PFC power fluxes are unavoidable, then it may be beneficial to rotate the RMP in time to reduce the root mean square (RMS) power loads. The downside of this is the potential thermal cycling of components and reduction in RMS NBI efficiency. Ultimately, the best case scenario is if both criteria can be optimised simultaneously—that is, if peak power flux correlates with global losses. Determining this is a key aim of this study.

Given their higher fusion power and stored energy, and their importance to the ITER mission, discharges from the Fusion Power Operation (FPO) stage are prioritised for investigation. As the plasma response to a given ECC perturbation is predicted to be similar in both the $Q = 5$ and $Q = 10$ variations of the

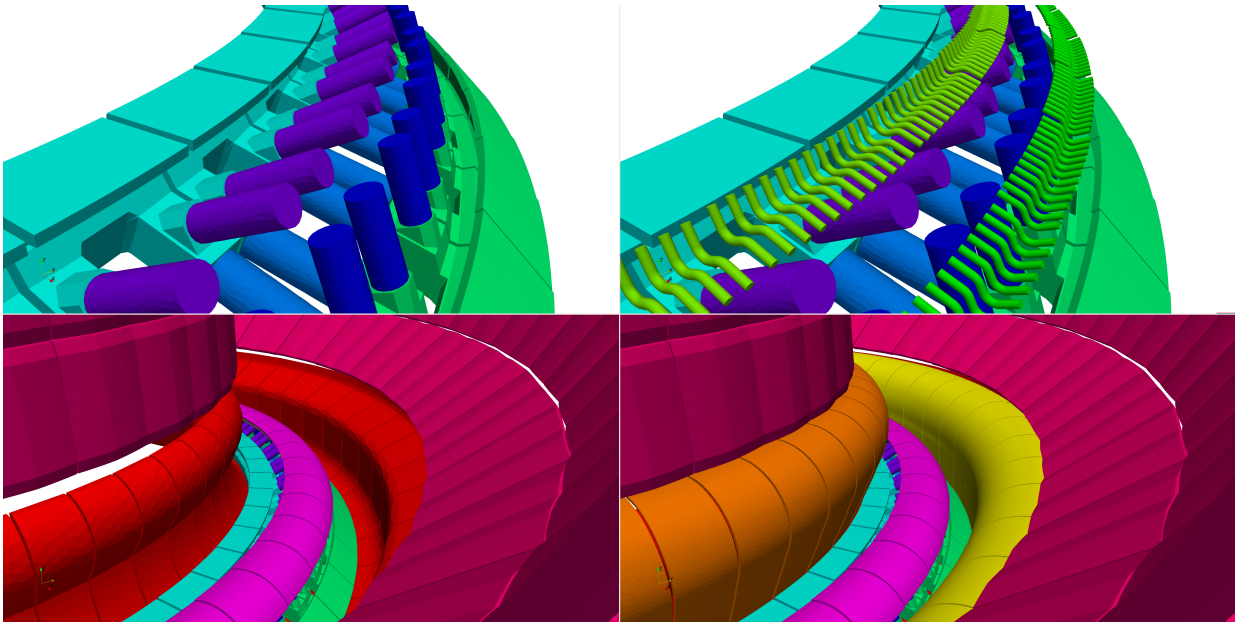

**Figure 6.** ITER mesh used by LOCUST, shown in four separate panels as groups of components are incrementally added. Clockwise from top left: Close-up of divertor inner and outer plates with inner, outer and horizontal supports; adding inner and outer underdome pipes; zoomed out with divertor base, first-wall and dome added; inner and outer baffle added. The underdome pipes, whilst shielded by the dome from the private flux region above, may be reached by fast-ions from the exposed sides. Fast-ions in this region may also strike the rounded vertical supports too. Colours match those used in Figure 10.

$I_\mathrm{p} = 15\,\mathrm{MA}$ deuterium-tritium FPO scenario, we focus here on studying the high-performance $Q = 10$ variation. Figure 7 shows the relevant plasma data for this discharge, including the $q$ profile which dictates edge stochasticity.

To adjust the phase and rotate the RMP whilst maintaining ELM suppression, the current in each ECC is oscillated whilst the relative current phase between each ECC row is fixed. To quantify the fast-ion transport in the likely extreme case, when ELM suppression is maximal, the optimal upper and lower row phases (those which maximise XPD) relative to the middle coil row were taken from [21][22]. All coils also passed the maximum current amplitude of 90 kAt. To generate a general yet realistic distribution of deposited neutral beam ions, both heating neutral beams (HNB1 and HNB2) were used, with HNB1 injecting off-axis and HNB2 injecting on-axis. The total injected NBI power is split equally between the beams—≈16.7 MW each. In future, ITER may install a third heating beam, HNB3, however this was ignored here. In this scenario, the calculated shine-through losses were extremely small and thus assumed to be negligible throughout.

### *4.1. Fast-ion transport*

Figure 8 shows the total measured power lost to PFCs from both beams as the RMP is rotated. ≈33,000 ($2^{15}$) markers (values greater than ≈8,000 ($2^{13}$) were sufficient for estimating global losses) were tracked over different values of absolute perturbation phase, represented in Figure 8 by middle row phase, $\Phi_\mathrm{m}$, whilst relative toroidal phase between coil rows ($\Delta\Phi_\mathrm{u} - \Delta\Phi_\mathrm{m}$ and $\Delta\Phi_\mathrm{l} - \Delta\Phi_\mathrm{m}$) was maintained. In the limit where the toroidal spectrum consists purely of the fundamental mode ($I(n) \sim \delta(n - n_0)$), the XPD remains constant as the perturbation rotates. However, in reality the inclusion of additional toroidal harmonics introduces a dependency on $\Phi_\mathrm{m}$. To see whether this has a noticeable effect on the fast-ions, we toggle the inclusion of the second harmonic, $n_1$. In the case where the sideband was removed, the remaining fundamental mode was artificially scaled up proportionally to mimic an ECC system capable of generating a pure $n = n_0$ RMP field. In reality, it is impossible for the ITER ECC system to generate a field with a fundamental mode of this amplitude.

Over a rotation cycle, the total measured losses vary by approximately $\pm 2.8 - 3.2\%$ points for $n_0 = 3$ and $\pm 1.7 - 2.1\%$ points for $n_0 = 4$—showing similar room for optimisation for both mode numbers. Whilst other work observes roughly double this variation for an individual beam in the $n = 3$ case [10], the toroidal separation of the beams means each is impacted by the perturbation in turn as it moves past, with losses from one beam lagging the other. Therefore the discrepency is likely smaller. Furthermore, the magnitude of global losses reflects those calculated in [15], and the absolute

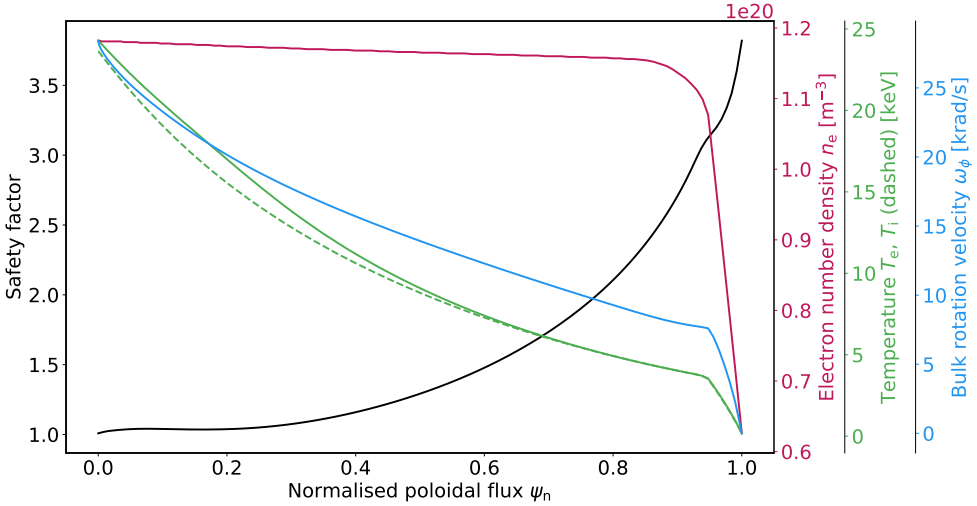


**Figure 7.** Plasma data representing the $Q = 10$ ITER DT scenario in `MARS-F` and subsequent `LOCUST` calculations. Included here are the safety factor $q$, electron and ion temperatures $T_e$ and $T_i$, electron density $n_e$ and rotation profile $\omega_\phi$ plotted against normalised poloidal flux $\psi_n$. The safety factor and rotation play a crucial role in determining the plasma response to RMPs, whilst the plasma density and temperature dictate the location of NBI-deposited fast-ions. The high plasma density leads to many fast-ions being deposited at the plasma edge, where the RMP amplitude is strongest.

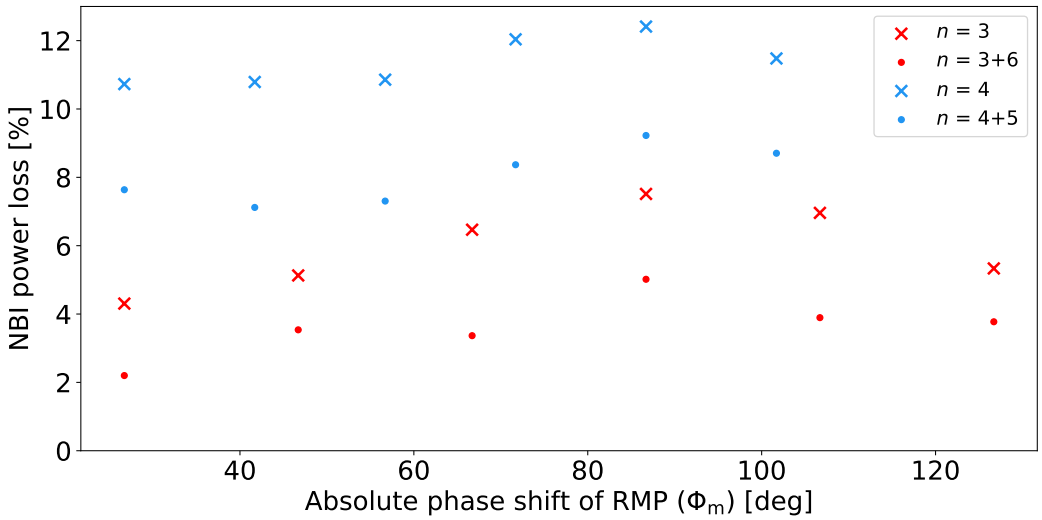


**Figure 8.** Global fast-ion losses to PFCs as a percentage of deposited beam power ($\approx 33$ MW) for different middle coil row phases, $\Phi_m$, whilst maintaining relative phases between all coil rows. This reflects the situation in which the RMP is rotated to spread the fast-ion power loads. Shown are results from fields with ($n = n_0 + n_1$) and without ($n = n_0$) the second harmonic. The scan begins at the point where the first middle coil is passing maximum current ($\Phi_m = 26.7°$). To relate the RMP field phase to the 3D system geometry, such as the toroidal localisation of the NBI deposition with respect to perturbation phase, $\Phi$ remains as defined in equation 1—that is, in the ITER machine coordinate system. Hence, absolute phase is varied through $360°/n_0$.

phases corresponding to minimal and maximal losses align well with those predicted in [10] ($\Phi \approx 22^\circ$ and $82^\circ$ respectively [31]). Interestingly, these phases also align across toroidal mode numbers and spectra, possibly because the upper and middle coil phases are similar in both the $n_0 = 3$ and $n_0 = 4$ fields when XPD is maximised. This alignment, as well as the difference between individual beam losses, suggests that the phase difference between peaks in ECC current and NBI deposition is a critical 3D parameter to tune if the field is to be fixed in place. However, it must be noted that the maximum losses do not occur when these peaks overlap (maximal HNB1 and HNB2 deposition occurs at $\phi = 58^\circ$ and $74^\circ$ respectively).

It is clear that $n_0 = 4$ fields are consistently worse for NBI heating efficiency, with minimum losses 6.4% and 4.9% points higher than their respective single and multi-harmonic $n_0 = 3$ equivalents. This could be due to the increased penetration of the stochastic layer, illustrated by the Poincare plots of Figure 9. Including the second harmonic is also crucial, as for both $n_0 = 3$ and $n_0 = 4$ fields it acts to significantly lowers global losses—by approximately 2.5% and 3.6% points respectively (by $\approx$ 1MW). Because of this, and the fact that pure $n = n_0$ fields are unrealistic, only fields including the second harmonic are studied from here.

### *4.2. Power loads*

It is now important to determine whether it is possible to optimise overall NBI heating efficiency whilst minimising localised PFC power fluxes. Figure 10 shows the component-resolved power loads for different toroidal mode spectra as a function of absolute RMP phase. Foremost, it can be seen that the relationship between power load and absolute phase is dependent upon the component and mode spectrum in question; some components do not experience peak power loads when global fast-ion losses are maximised—even in pure $n = n_0$ fields, where rotation does not affect the field structure. Hence the rotation and spectrum of an RMP each act not only to scale but also redistribute fast-ion losses.

It is therefore important to examine the spatial distribution of lost particles, which is plotted in Figure 11 for a single phase over the perturbation amplitude evaluated at the plasma edge. Whilst we do not aim to identify the main loss or redistribution mechanisms, we note the influence of particle orbit topology by highlighting the strong correlation between loss location and particle pitch angle ($v_\parallel/v$, as measured against plasma current direction, which is typically clockwise in ITER). This correlation persists as the perturbation phase changes. In addition, the loss pattern, which remains field-aligned and $n_0$-fold toroidally symmetric, rotates with the perturbation without significantly changing shape; any redistribution is observed to occur within the length scales of the loss footprint. This is likely why FILDs detect oscillations in fast-ion losses as RMPs are rotated in experiments.

To identify hotspots within the footprint, and determine whether they persist, redistribute, or fluctuate, the number of markers was increased to approximately two million ($2^{21}$), and 3D power loads were resolved at the sub-component level. These are shown for $n = 3+6$ fields in a top-down view in Figure 12 over the same phases used for Figure 8. For $n = 3+6$ fields, the power load footprint is largely contained within the divertor and first-wall regions, specifically panels near the outboard mid-plane - as can be seen in Figure 11. The same can be said for the $n = 4 + 5$ field; Figure 13 shows similar patterns, except a new footprint is introduced on the outboard ceiling first-wall panels.

Like the loss pattern, for both mode numbers the power load adheres to the perturbation as it rotates. However, first-wall power loads are toroidally asymmetric—mostly limited to sections further from the HNB ports. These are not shine-through losses (LOCUST only tracks deposited ions, and the regions are blocked by the central column). Figures 14 and 15 show these particular power loads from outside the machine. It can now be seen more clearly that, as the footprint rotates and first-wall panels are struck in-turn, specific first-wall segments attract far higher power loads. Crucially, the power loads here do not persist throughout the rotation, meaning that, for both mode numbers, first-wall RMS power loads could be reduced by RMP rotation. The only persistent loads are limited to specific divertor regions shown below.

Further close-ups of these first-wall loads are displayed in Figures 16 and 17, which highlight panels diametrically opposite to the HNB ports. Here it can be seen that the peak power loads strike specific sides of the bevelled panels—typically the side facing the HNB ports. Whilst high, the maximum heatloads of approximately 0.5-0.7 $\mathrm{MWm^{-2}}$ are tolerable in these locations. The wall panels in question correspond to blanket modules 14 and 15 [32] which are designated "enhanced heat flux" panels [33], designed to accommodate up to $\approx 5\,\mathrm{MWm^{-2}}$ (compared to "normal heat flux" panels rated for 1-2 $\mathrm{MWm^{-2}}$). As can be seen, the peak power loads can be reduced—and re-positioned—by switching toroidal mode number.

To understand whether rotation is necessary to reduce RMS power loads, the peak power load to the first wall is plotted at various RMP phases in Figure 18. In either case, rotation of the RMP should significantly reduce the peak first-wall power load. For $n_0 = 3$ fields,

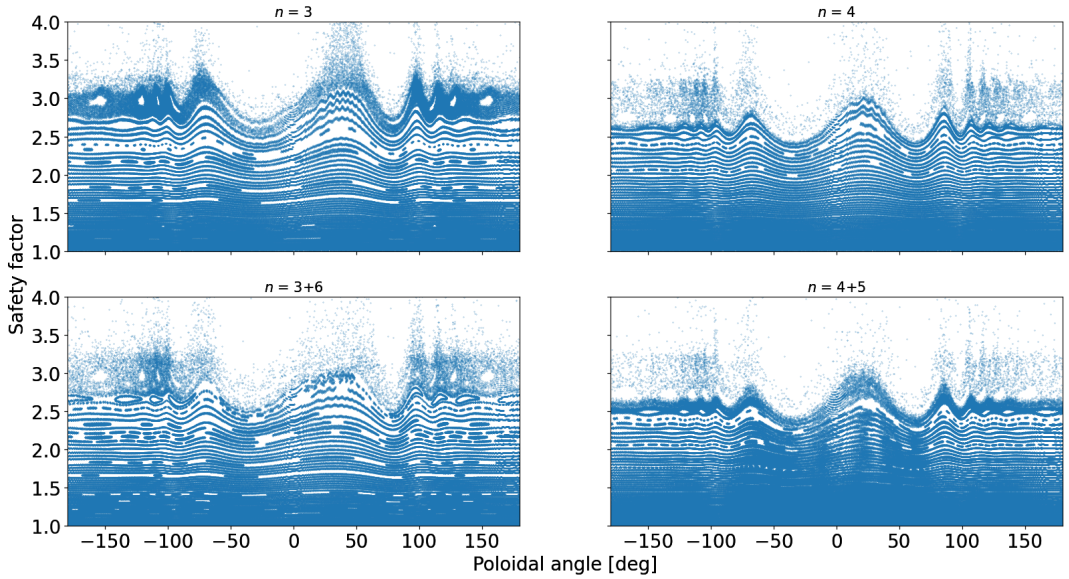


**Figure 9.** Poincare maps for fields at the same $\Phi_m$ but different toroidal mode numbers and spectra, plotted against safety factor $q$ and poloidal angle $\theta$. The maps are evaluated at $\phi = 60°$. The patterns near $\theta = 0°$ are due to the transform from rectilinear coordinates. Fields with one harmonic have been artificially scaled up to correspond to an ECC system capable of creating pure-$n_0$ fields. In this case, the RMP penetration is not increased by the secondary harmonic, but it is possible to see that it still changes the field structure at the edge.

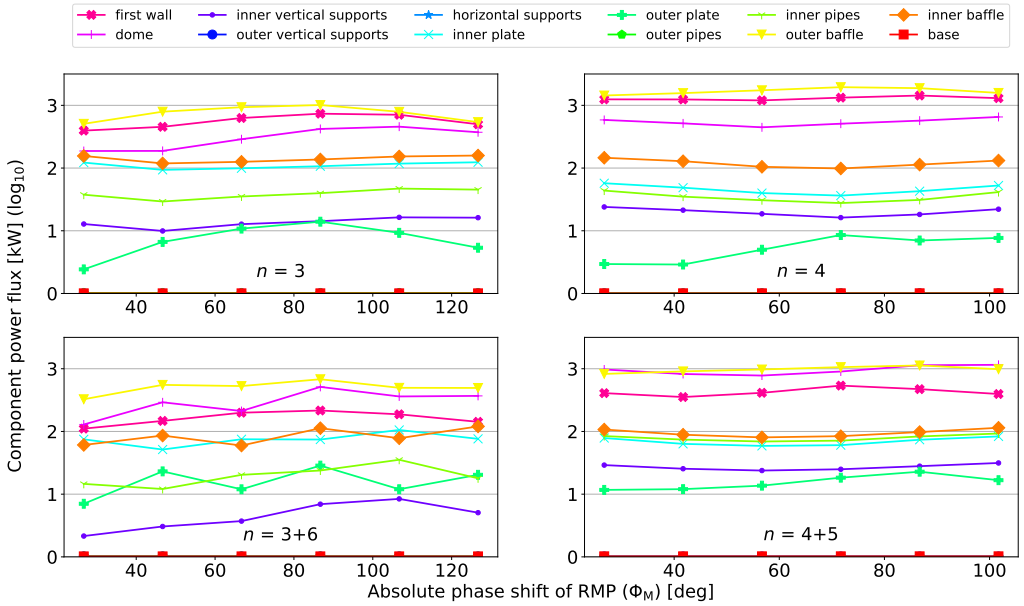


**Figure 10.** Power loads to various tokamak first-wall components as a function of absolute toroidal perturbation phase for different RMP mode spectra at 90 kAt coil current amplitude. Components which received negligible power flux are denoted at the bottom (base, outer vertical supports, horizontal supports and outer pipes). Colours and components correspond to those labelled in Figure 6. Where traces do not follow the same pattern exhibited by global losses in Figure 8, the field is implied to redistribute fast-ions amongst components.

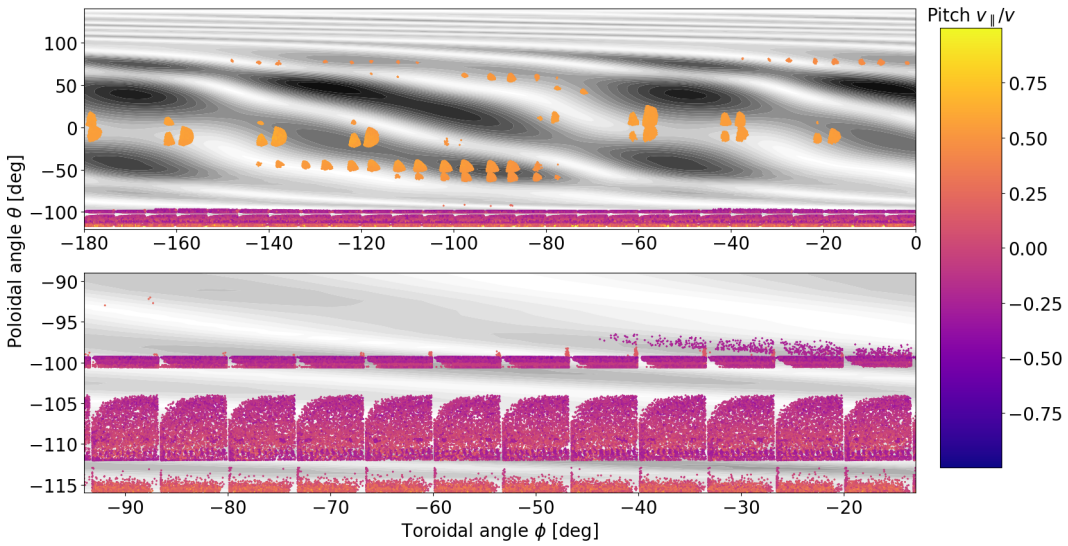


**Figure 11.** Two views of an $n = 3 + 6$ perturbation evaluated at $\psi_n = 0.99$ with lost markers plotted at their final poloidal angle $\theta$ and toroidal angle $\phi$ locations, coloured according to final pitch $\lambda$. The particle loss pattern adheres to the perturbation as it is rotated toroidally.

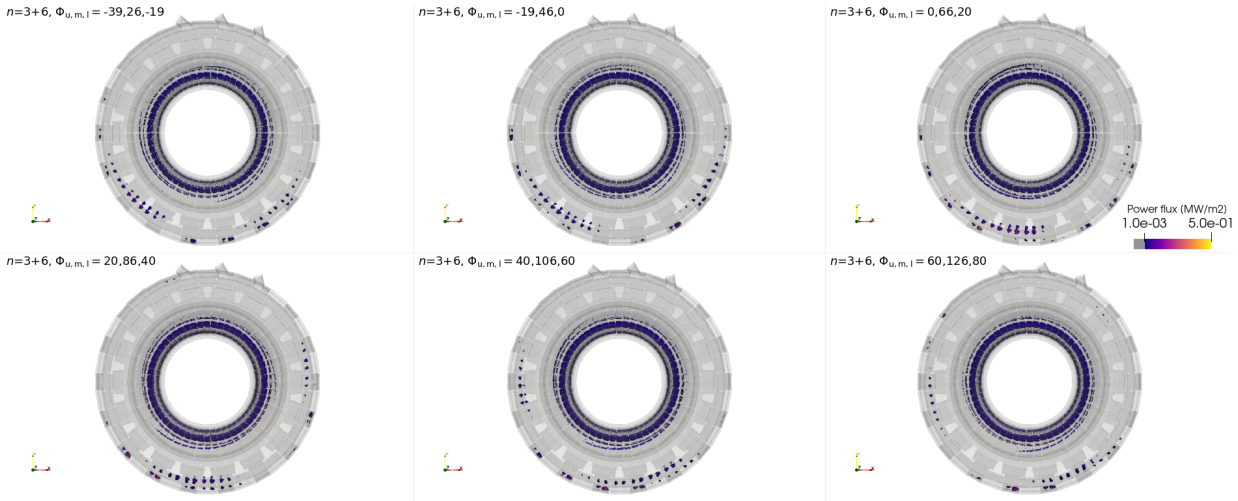


**Figure 12.** Top-down view of the first-wall with power loads rendered in colour. Ports for the three HNBs protrude from the vessel at the top, near $\phi = 90°$, whilst first-wall panels opposite attract a relatively high power load. From this view, the $n_0$-fold symmetric shape of the power load can be seen throughout the rotation cycle. Untouched surfaces are rendered semi-transparent.

peak power flux correlates well with the global fast-ion losses shown in Figure 8, potentially making RMP rotation unnecessary. However, the same cannot be confidently said for $n_0 = 4$ fields; this is only true once the sideband is included, which changes the phase at which global losses are minimised (from $\Phi_m = 26°$ to $\Phi_m = 41°$). This is corroborated when considering the divertor region, shown in Figures 19 and 20. Like the first-wall, peak power loads to the divertor dome and outer baffle oscillate with global losses in the $n = 3+6$ case. Whereas in the $n = 4+5$ case, for example on the dome, peak power loads only redistribute and can even persist; when global losses are minimal ($\Phi_m = 41°$), higher fluxes remain on the inboard side of the dome structure and on the outer baffle.

Overall, $n_0 = 4$ fields consistently lead to higher divertor power loads across all components. And like the bevelled first-wall tiles, the orientation and subtle geometry of PFCs can greatly affect the power received. This is apparent specifically on the dome and outer baffle, where breaks in shadowing and regions with discontinuities, such as gaps between divertor

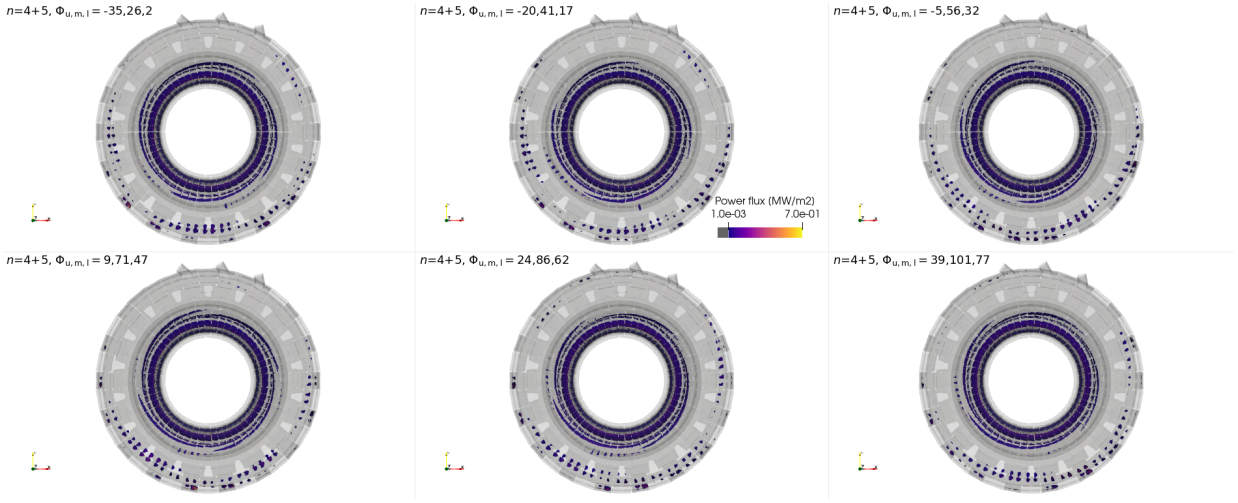


**Figure 13.** Same view used in Figure 12 but for an $n_0 = 4$ RMP field. A similar behaviour to the $n_0 = 4$ field can be seen.

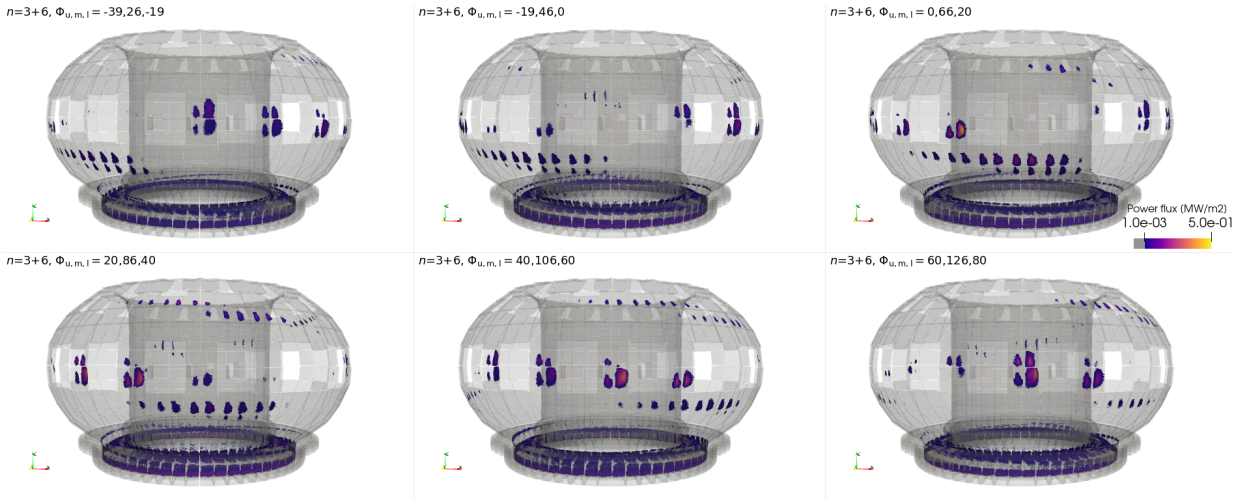


**Figure 14.** Fast-ion power loads as viewed outside the vessel. The wall panels closest to the camera are located opposite to the HNB ports. Gaps between panels exist in places where diagnostic or entry ports are located. Untouched surfaces are rendered semi-transparent.

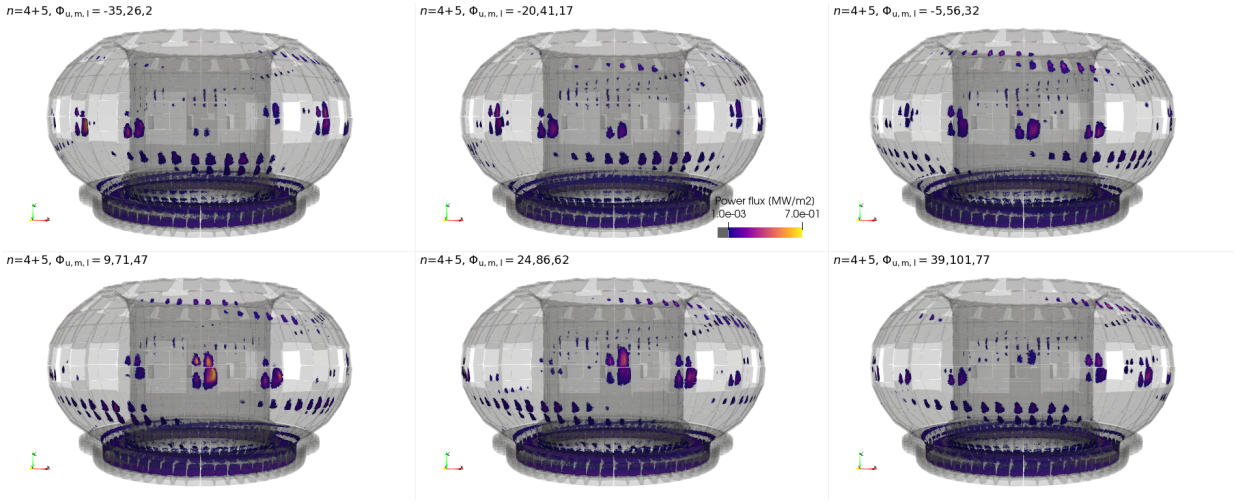


**Figure 15.** Same view as Figure 14 but for an $n_0 = 4$ RMP field. Not only are the power loads larger in area and more intense at their peak, but additional footprints are created near the ceiling of the reactor chamber.

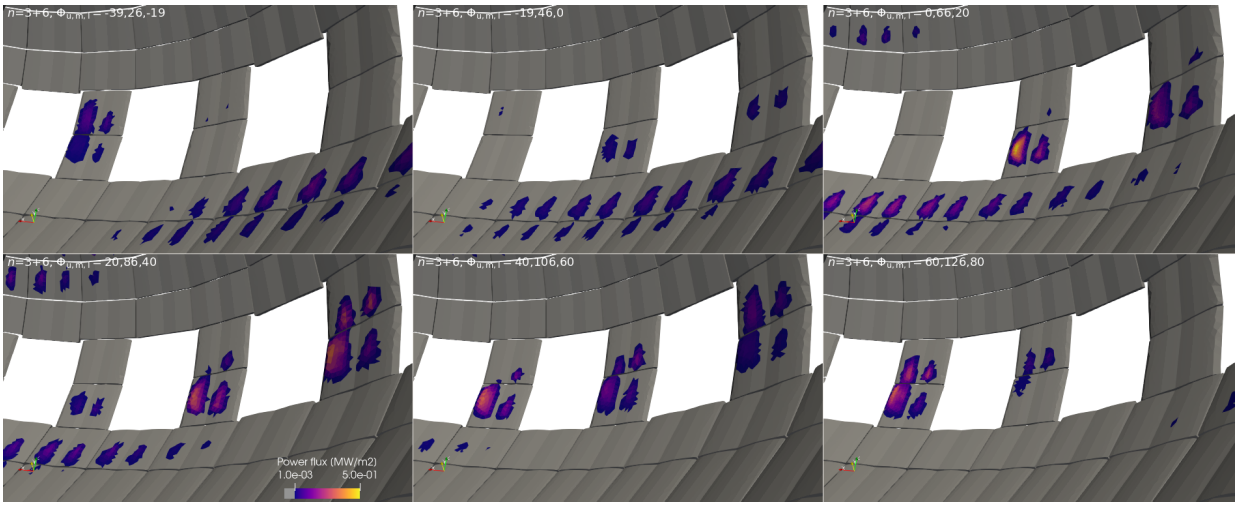


**Figure 16.** Fast-ion power loads shown from the divertor looking upward toward the wall tiles located opposite to the HNB ports. The power load on a given wall panel is heavily influenced by the panel geometry, with peak heat fluxes typically located on the side facing the neutral beam ports.

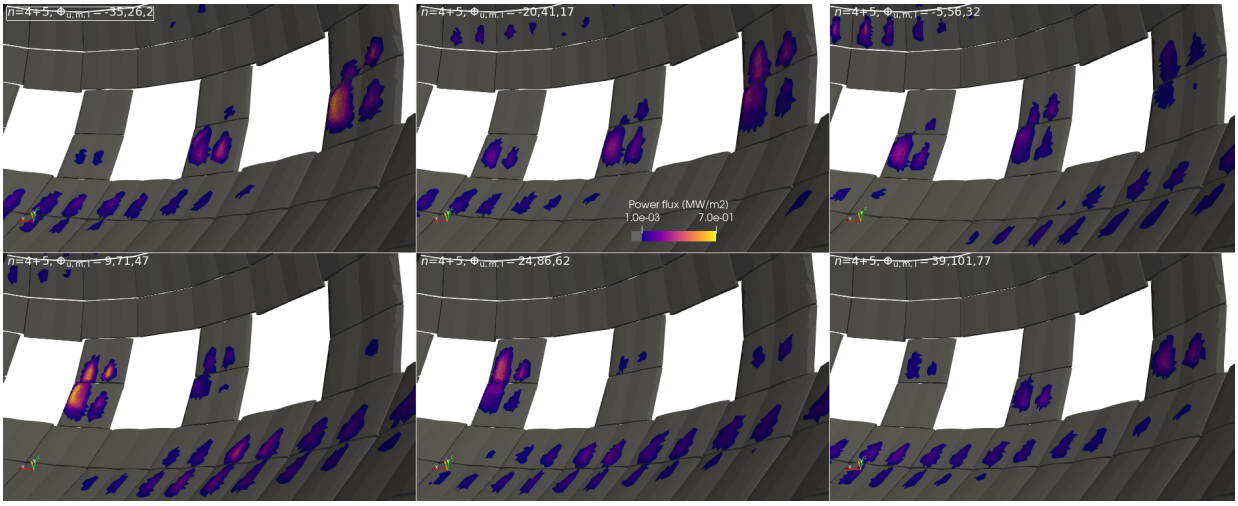


**Figure 17.** Same view and wall model used above in Figure 16 but for an $n_0 = 4$ RMP field. The panel columns which avoid peak power loads here instead receive peak loads in Figure 16 above for $n_0 = 3$ fields. The additional ceiling power loads can also be seen.

cassettes, attract particularly high power loads due to the low angle of incidence. Rotation is unlikely to reduce these power loads between the cassette domes in the $n_0 = 4$ case, again making optimisation less straightforward. Nevertheless, the divertor region receives manageable power loads in any case.

The same is true for vulnerable components, such as the under-dome cooling pipes; Figure 21 shows these for the two phases which exhibit the highest power loads, which rarely exceed $0.25\,\mathrm{MWm}^{-2}$. Again, these are sensitive to the local geometry—in this case, the curved edges of the inner support legs and gaps between divertor cassette gaps which highlight endmost cooling pipes. The high power loads on the individual surface triangles of the underdome pipes are due to a lack of marker statistics, however the presence of more marker hits in the $n = 4 + 5$ case signifies an increased power load.

## 5. Summary

The LOCUST code has been applied to studying fast-ion transport in ITER. In particular, transport due to the ITER ECC system was calculated as the system was cycled to toroidally rotate the imposed RMP. Initially, the 3D magnetic field model in LOCUST was verified against the SPIRAL code by studying fast-ion transport in an ITER-similar RMP experiment. Both codes sufficiently well to conclude that the 3D magnetic field model in LOCUST is implemented correctly. For its convergence, centimetre perturbation grid sizes and multiple toroidal harmonics were found to be highly

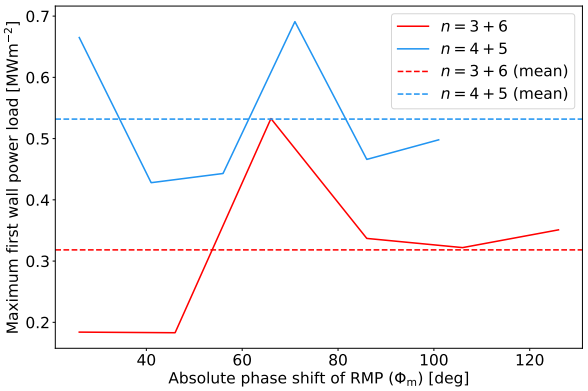


**Figure 18.** Maximum power load reaching the first-wall at a single surface mesh triangle for various RMP phases and toroidal mode numbers. The average value is also displayed, which is much lower than the peak power flux over the total rotation cycle—demonstrating that the intensity of hotspots can be significantly reduced if the RMP field is rotated.

important. However, further efforts to validate the 3D magnetic field models used in various fast-ion codes against existing RMP experiments, such as those carried out by the ITPA-EP group, remain highly important. The benefits of this type of activity are clear, as the results herein exhibit differences alongside similarities to equivalent studies.

After testing, LOCUST was applied to study global and local fast-ion losses in the $Q = 10$ ITER scenario. Depending on their spectra and phase, the RMP fields were shown to reduce overall NBI heating efficiency by $\approx 2-12\%$ (0.7-4.0 MW), though each beam is affected in turn whilst the RMP rotates. Toroidal mode number was found to be the most sensitive parameter for controlling fast-ion confinement, however $n_0 = 4$ modes were found to be consistently worse for both global fast-ion confinement and PFC power loads. By adjusting the phase of the RMP, NBI heating efficiency can be increased by 1.7-3.2%, whilst the fast-ion power loads can be redistributed. As such, rotating the RMP is highly likely to reduce the RMS power flux to most components. This is particularly true for the first wall, where mid-plane tiles diametrically opposite to the HNB injection ports attract relatively intense power loads at some RMP phases. However, for $n_0 = 3$ fields, the optimal solution may be simply to fix the absolute RMP phase at the point where the first middle coil passes maximum current—as both global fast-ion losses and PFC power flux are minimised here. In practice, the results here may be confirmed by the relatively low-power diagnostic neutral beam in conjunction with available diagnostics [26]. Overall, even in the worst-case scenario, power loads should be within the design limits of the ITER first-wall and divertor.

The sensitivity of power loads to orbit topology makes it important to study the effects of 3D plasma edge displacement ($\sim$cms) on the initial neutral beam distribution. This is especially true given that most fast-ions are born close to the trapped-passing boundary. Likewise, the increased flux between cassette gaps suggests that, in reality, power loads could be greatly affected by PFC misalignment or localised melting. Integrated simulations which include components to capture melting dynamics [34] and re-meshing tools [35], such as the system employed in [36], could prove important follow-up work.

In summary, substantial gains in NBI and overall plant efficiency can be achieved with relatively inconsequential adjustments to the ECC system operation. The results here show that, if these adjustments are made, then, even at the maximum level of ELM suppression, fast-ion power loads are unlikely to exceed the engineering limits of the PFCs for $n_0 = 3$ fields. However, if ELM suppression can be achieved with a smaller applied perturbation, new avenues emerge for further optimisation of ECC operation—namely, the lowering of ECC current amplitude and the adjustment of relative phase between upper and lower coil rows [26]. This problem is highly suited for study with LOCUST, as well as other novel algorithms, such as the recent backward Monte Carlo approach to solving the adjoint problem [37].

## 6. Acknowledgements

*The project was partly undertaken on the ITER Organization's Titan GPU server within its Scientific Data Computing Centre (SDCC).*
This project was undertaken on the Viking Cluster, which is a high performance compute facility provided by the University of York. We are grateful for computational support from the University of York High Performance Computing service, Viking and the Research Computing team. Additional thanks are also owed to Lucía Sanchís and Todd Evans for their help and valuable discussions.
*The work presented in this publication has been carried out under a joint PhD project among the ITER Organization, UKAEA and the University of York and has received financial support from the ITER Organization under Collaboration Agreement LEGAL6411249v1*
*The views and opinions expressed herein do not necessarily reflect those of the European Commission. The views and opinions expressed herein do not necessarily reflect those of the ITER Organization.*

## References

[1] Fritz Wagner, G Becker, K Behringer, D Campbell, A Eberhagen, W Engelhardt, G Fussmann, O Gehre,

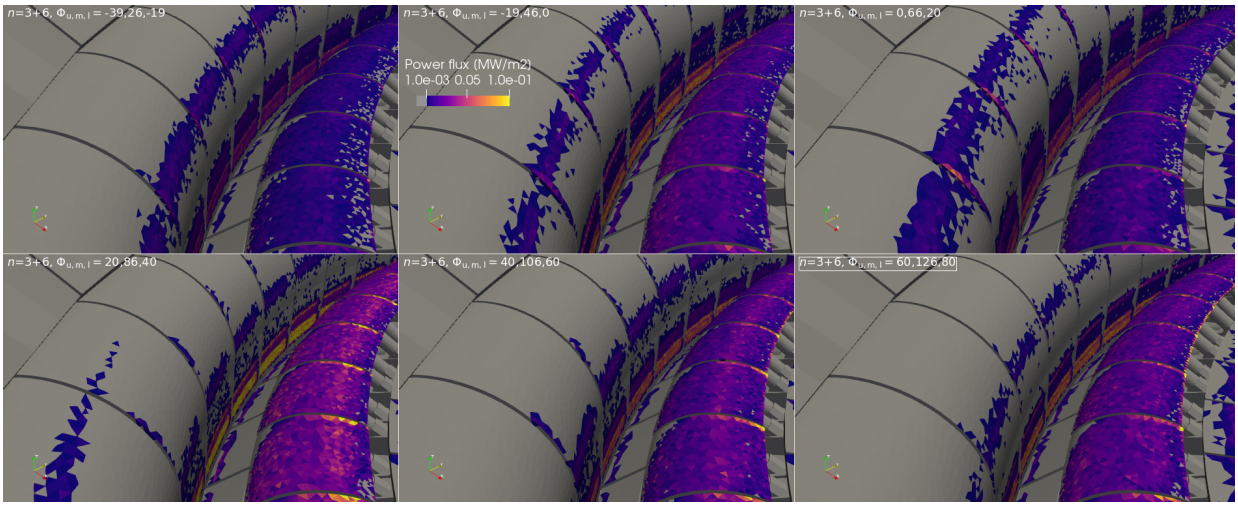


**Figure 19.** Fast-ion power loads looking down onto the divertor dome for an $n_0 = 3$ field. Here it can be seen that maximal power loads correlate well to maximum global losses shown in Figure 8. The cassette gaps on the outer baffle and divertor dome can attract power loads that approach the peak.

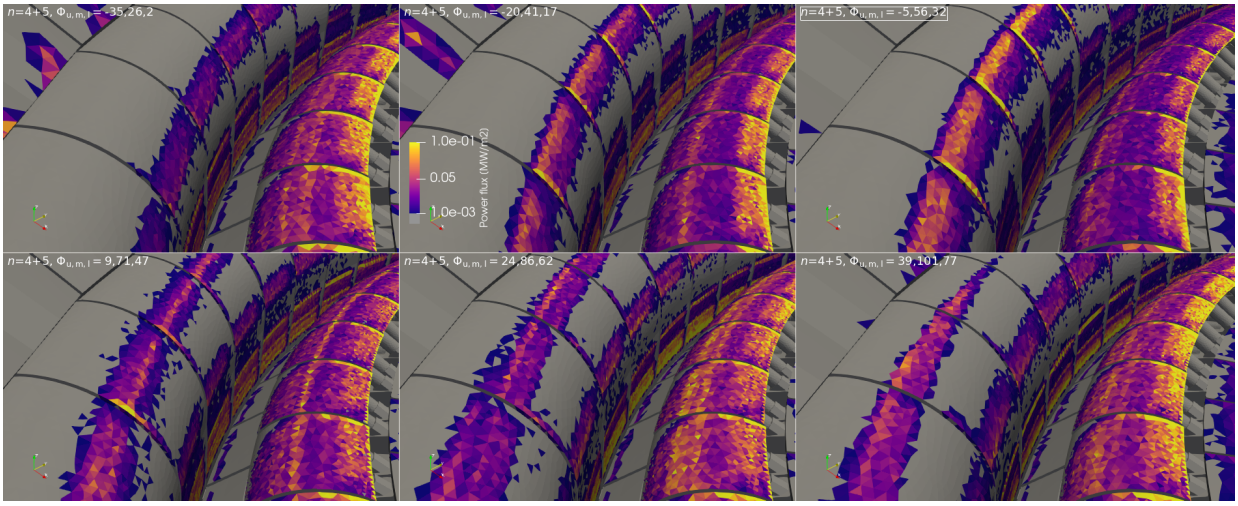


**Figure 20.** Same view as Figure 19 but for an $n_0 = 4$ RMP field. Unlike $n_0 = 3$ fields, peak power loads are located in multiple regions, such as cassette gaps, the outer baffle and inboard side of the dome. In some of regions, peak power loads persist throughout the RMP cycle.

J Gernhardt, G v Gierke, et al. Regime of improved confinement and high beta in neutral-beam-heated divertor discharges of the asdex tokamak. *Physical Review Letters*, 49(19):1408, 1982.

[2] ITER Organization. Iter research plan within the staged approach. *ITER technical report ITR-18-003*, 2018.

[3] A Loarte, G Huijsmans, S Futatani, LR Baylor, TE Evans, DM Orlov, O Schmitz, M Becoulet, P Cahyna, Y Gribov, et al. Progress on the application of elm control schemes to iter scenarios from the non-active phase to dt operation. *Nuclear Fusion*, 54(3):033007, 2014.

[4] TE Evans. Resonant magnetic perturbations of edge-plasmas in toroidal confinement devices. *Plasma Physics and Controlled Fusion*, 57(12):123001, 2015.

[5] M De Rover, AMR Schilham, A Montvai, and NJ Lopes Cardozo. Test particle transport in perturbed magnetic fields in tokamaks. *Physics of Plasmas*, 6(6):2443–2451, 1999.

[6] TE Evans, I Joseph, RA Moyer, ME Fenstermacher, CJ Lasnier, and LW Yan. Experimental and numerical studies of separatrix splitting and magnetic footprints in diii-d. *Journal of Nuclear Materials*, 363:570–574, 2007.

[7] Michael A Van Zeeland et al. Fast ion transport during applied 3D magnetic perturbations on DIII-D. *Nuclear Fusion*, 55(7):073028, 2015.

[8] L Sanchis, M Garcia-Munoz, A Snicker, DA Ryan, David Zarzoso, Lin Chen, J Galdon-Quiroga, M Nocente, JF Rivero-Rodriguez, M Rodriguez-Ramos, et al. Characterisation of the fast-ion edge resonant transport layer induced by 3d perturbative fields in the asdex upgrade tokamak through full orbit simulations. *Plasma Physics and Controlled Fusion*, 61(1):014038, 2018.

[9] Konsta Särkimäki. Efficient and rigorous evaluation of fast particle losses in non-axisymmetric tokamak plasmas. *Nuclear Fusion*, 60(3):036002, 2020.

[10] L Sanchis, M Garcia-Munoz, Eleonora Viezzer, Alberto Loarte, L Li, YQ Liu, A Snicker, L Chen, Fulvio Zonca, SD Pinches, et al. Optimizing beam-ion confinement

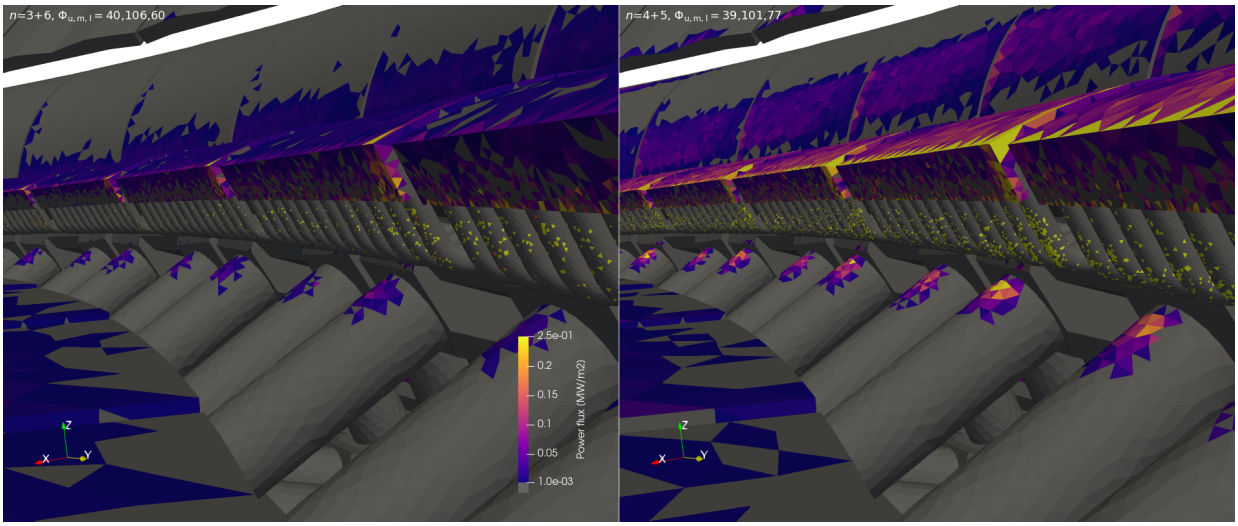


**Figure 21.** View of divetor power loads for $n_0 = 3$ and $n_0 = 4$ fields when power loads are maximal, looking towards the outboard side from the inner divertor plate. Shown are the inner support legs, the inboard edges of the divertor dome structure and its cooling pipes, and a portion of the upper region of the outer baffle. Whilst the number of markers striking the pipes is small, the edge-most pipes exhibit an increased number of hot surface triangles due to the gaps in the divertor dome.

in iter by adjusting the toroidal phase of the 3d magnetic fields applied for elm control. *Nuclear Fusion*, 61(4):046006, 2021.

[11] Jari others Varje. Effect of plasma response on the fast ion losses due to elm control coils in ITER. *Nuclear Fusion*, 56(4):046014, 2016.

[12] Konsta Särkimäki et al. Mechanics of elm control coil induced fast particle transport in ITER. *Nuclear Fusion*, 58(7):076021, 2018.

[13] Eric Nardon, P Cahyna, S Devaux, A Kirk, A Alfier, E De La Luna, G De Temmerman, P Denner, T Eich, Thomas Gerbaud, et al. Strike-point splitting induced by external magnetic perturbations: observations on jet and mast and associated modelling. *Journal of nuclear materials*, 415(1):S914–S917, 2011.

[14] RS Hemsworth, D Boilson, P Blatchford, M Dalla Palma, G Chitarin, HPL De Esch, F Geli, M Dremel, J Graceffa, D Marcuzzi, et al. Overview of the design of the iter heating neutral beam injectors. *New Journal of Physics*, 19(2):025005, 2017.

[15] R Akers, B Colling, J Hess, Y Liu, A Turner, S Äkäslompolo, J Varje, K Särkimäki, SD Pinches, and M Singh. High fidelity simulations of fast ion power flux driven by 3d field perturbations on iter. Technical report, 2016.

[16] R A Pitts, A Kukushkin, A Loarte, A Martin, M Merola, C E Kessel, V Komarov, and M Shimada. Status and physics basis of the ITER divertor. *Physica Scripta*, T138:014001, dec 2009.

[17] S.H. Ward, R. Akers, A.S. Jacobsen, P. Ollus, S.D. Pinches, E. Tholerus, R.G.L. Vann, and M.A. Van Zeeland. Verification and validation of the high-performance lorentz-orbit code for use in stellarators and tokamaks (LOCUST). *Nuclear Fusion*, 61(8):086029, jul 2021.

[18] GJ Kramer et al. A description of the full-particle-orbit-following spiral code for simulating fast-ion experiments in tokamaks. *Plasma Physics and Controlled Fusion*, 55(2):025013, 2013.

[19] SC Jardin et al. Multiple timescale calculations of sawteeth and other global macroscopic dynamics of tokamak plasmas. *Computational Science & Discovery*, 5(1):014002, 2012.

[20] EF Daly, K Ioki, A Loarte, A Martin, A Brooks, P Heitzenroeder, M Kalish, C Neumeyer, P Titus, Y Zhai, et al. Update on design of the iter in-vessel coils. *Fusion Science and Technology*, 64(2):168–175, 2013.

[21] L Li, YQ Liu, A Loarte, SD Pinches, A Polevoi, Y Liang, and FC Zhong. Modeling 3d plasma boundary corrugation and tailoring toroidal torque profiles with resonant magnetic perturbation fields in iter. *Nuclear Fusion*, 59(9):096038, 2019.

[22] LYQL Li, YQ Liu, A Loarte, SD Pinches, A Polevoi, and FC Zhong. Elm control optimization for various iter scenarios based on linear and quasi-linear figures of merit. *Physics of Plasmas*, 27(4):042510, 2020.

[23] YQ Liu, Anders Bondeson, Carl-Magnus Fransson, Bengt Lennartson, and Claes Breitholtz. Feedback stabilization of nonaxisymmetric resistive wall modes in tokamaks. i. electromagnetic model. *Physics of Plasmas*, 7(9):3681–3690, 2000.

[24] Carl-Magnus Fransson, Bengt Lennartson, Claes Breitholtz, A Bondeson, and YQ Liu. Feedback stabilization of nonaxisymmetric resistive wall modes in tokamaks. ii. control analysis. *Physics of Plasmas*, 7(10):4143–4151, 2000.

[25] Gregorij V Pereverzev and PN Yushmanov. Astra. automated system for transport analysis in a tokamak. 2002.

[26] S.H. Ward, R. Akers, A. Loarte, L. Li, Y.Q. Liu, S.D. Pinches, A. Polevoi, and R.G.L. Vann. Optimising fast-ion transport due to ELM-control coils in ITER discharges with LOCUST-GPU (submitted). *Nuclear Fusion*, 2022.

[27] C Chrystal, BA Grierson, GM Staebler, CC Petty, WM Solomon, JS DeGrassie, KH Burrell, T Tala, and A Salmi. Predicting rotation for iter via studies of intrinsic torque and momentum transport in diii-d. *Physics of Plasmas*, 24(5):056113, 2017.

[28] L Li, YQ Liu, A Loarte, SD Pinches, A Polevoi, and FC Zhong. Toroidal modeling of resonant magnetic perturbations in preparation for the initial phase of ITER operation. *Nuclear Fusion*, 60(1):016013, 2019.

[29] O. Asunta, J. Govenius, R. Budny, M. Gorelenkova, G. Tardini, T. Kurki-Suonio, A. Salmi, and S. Sipilä.

Modelling neutral beams in fusion devices: Beamlet-based model for fast particle simulations. *Computer Physics Communications*, 188:33–46, 2015.

[30] MA Van Zeeland et al. Modulation of prompt fast-ion loss by applied n=2 fields in the DIII-D tokamak. *Plasma Physics and Controlled Fusion*, 56(1):015009, 2013.

[31] Lucía Sanchís. personal communication.

[32] R.A. Pitts, S. Carpentier, F. Escourbiac, T. Hirai, V. Komarov, A.S. Kukushkin, S. Lisgo, A. Loarte, M. Merola, R. Mitteau, A.R. Raffray, M. Shimada, and P.C. Stangeby. Physics basis and design of the iter plasma-facing components. *Journal of Nuclear Materials*, 415(1, Supplement):S957–S964, 2011. Proceedings of the 19th International Conference on Plasma-Surface Interactions in Controlled Fusion.

[33] R. Mitteau, B. Calcagno, P. Chappuis, R. Eaton, S. Gicquel, J. Chen, A. Labusov, A. Martin, M. Merola, R. Raffray, M. Ulrickson, and F. Zacchia. The design of the iter first wall panels. *Fusion Engineering and Design*, 88(6):568–570, 2013. Proceedings of the 27th Symposium On Fusion Technology (SOFT-27); Liège, Belgium, September 24-28, 2012.

[34] Emil Thorén, Svetlana Ratynskaia, Panagiotis Tolias, Richard A Pitts, et al. The memos-u code description of macroscopic melt dynamics in fusion devices. *Plasma Physics and Controlled Fusion*, 63(3):035021, 2021.

[35] L Kos, RA Pitts, G Simič, M Brank, H Anand, and W Arter. Smiter: A field-line tracing environment for iter. *Fusion Engineering and Design*, 146:1796–1800, 2019.

[36] Jonathan Coburn, Michael Lehnen, Richard A Pitts, Gregor Simic, Francisco Javier Artola, Emil Thorén, Svetlana Ratynskaia, Kenzo Ibano, Matic Brank, Leon Kos, et al. Energy deposition and melt deformation on the iter first wall due to disruptions and vertical displacement events. *Nuclear Fusion*, 2021.

[37] Eero Hirvijoki. Eliminating poor statistics in monte-carlo simulations of fast-ion losses to plasma-facing components and detectors. *arXiv preprint arXiv:1905.04952*, 2019.